Diffraction of deep-water solitons

Filip Novkoski,[1,2,*] Loïc Fache,[1,3,†] Félicien Bonnefoy,[4] Guillaume Ducrozet,[4] Jason Barckicke,[1] François Copie,[3] Pierre Suret,[3] Eric Falcon,[1] and Stéphane Randoux[3]

[1] *Université Paris Cité, CNRS, Matière et systèmes complexes, F-75013 Paris, France*
[2] *PULS, Institute for Theoretical Physics, FAU Erlangen-Nürnberg, 91058, Erlangen, Germany*
[3] *Univ. Lille, CNRS, UMR 8523 - PhLAM - Physique des Lasers Atomes et Molécules, F-59 000 Lille, France*
[4] *Nantes Université, École Centrale Nantes, CNRS, LHEEA, UMR 6598, F-44 000 Nantes, France*

Solitons are localized nonlinear wave packets that propagate without spreading because nonlinearity balances dispersion. Their robustness is well understood in effectively one-dimensional (1D) systems, but introducing additional spatial dimensions is generally expected to destabilize them or destroy their coherent character. Here we experimentally investigate how deep-water gravity-wave solitons behave when a controlled transverse degree of freedom is introduced via diffraction. Using a large-scale water-wave facility, we generate solitonic wave packets whose transverse structure is imposed across a segmented wavemaker through either a sharp slit or a smooth Gaussian apodization. The resulting two-dimensional wave fields are measured with high spatial resolution. We find that diffraction strongly reshapes the transverse structure of the wave packet while its longitudinal dynamics retain clear signatures of soliton coherence. Numerical simulations based on the hyperbolic nonlinear Schrödinger equation accurately reproduce the experimental evolution. Furthermore, nonlinear spectral analysis based on the inverse scattering transform reveals the persistence of soliton dynamics over a significant portion of the wave field. At the same time, the measured transverse profiles are quantitatively described by classical diffraction theory over a broad range of conditions. These results provide an experimental characterization of how coherent structures inherited from an integrable 1D system evolve under controlled departures from one-dimensionality, revealing the robustness of soliton dynamics in the presence of transverse diffraction.

Diffraction is a fundamental and universal consequence of wave propagation. Its quantitative description was instrumental in establishing the wave nature of light, most notably through Fresnel's formulation of wave theory based on Huygens' principle [1]. Diffraction arises whenever a wave encounters spatial variations in impedance or boundary conditions, independent of the specific physical system. Accordingly, diffraction is observed not only in optics [2] but also in other wave systems, such as acoustic waves [3], elastic waves [4], or surface water waves [5].

For water waves, diffraction plays an important role in coastal hydrodynamics, particularly in the interaction of sea waves with engineered structures such as breakwaters [6]. The effects of edges, apertures, and gaps have therefore been investigated extensively, both theoretically [6–10] and experimentally [11, 12]. Most of these studies, however, have been conducted within the framework of linear wave theory. In realistic ocean conditions, nonlinear effects become significant and can lead to the emergence of coherent localized structures such as envelope solitons and breathers [13, 14]. These nonlinear wave packets have attracted considerable attention because of their connection to modulational instability and rogue-wave formation [15, 16]. Despite their robustness under essentially one-dimensional (1D) propagation, relatively little is known experimentally about how solitons behave when subjected to genuinely two-dimensional (2D) dynamics.

Deep-water gravity waves provide a particularly suitable framework for addressing this question. Under weakly nonlinear and narrow-band assumptions, their 1D dynamics are described by the focusing nonlinear Schrödinger equation (1D-NLSE) [17, 18]. This equation is integrable and possesses soliton solutions that can be characterized exactly through the inverse scattering transform (IST) [19–21]. Many of its properties have been successfully investigated experimentally, including modulational instability [22], integrable turbulence [23], and soliton-gas dynamics [24–26]. In these studies, coherent structures owe their remarkable stability to the balance between dispersion and nonlinearity embodied by the integrable NLSE.

The situation changes fundamentally when an additional spatial dimension is introduced. In that case, the appropriate weakly nonlinear model becomes the hyperbolic nonlinear Schrödinger equation (HNLSE), which is no longer integrable and incorporates transverse diffraction as an intrinsic part of the dynamics [27, 28]. As a result, coherent structures originating from the 1D limit can deform, spread, or undergo transverse instabilities [29–31]. This issue is relevant far beyond hydrodynamics: integrable 1D equations such as the 1D-NLSE provide remarkably accurate descriptions of coherent wave dynamics in systems ranging from optical fibers to Bose–Einstein condensates, while higher-dimensional effects can be present and may modify the dynamics predicted by 1D models. Investigating

* filip.novkoski@fau.de
† loic-joseph.fache@u-pariscite.fr

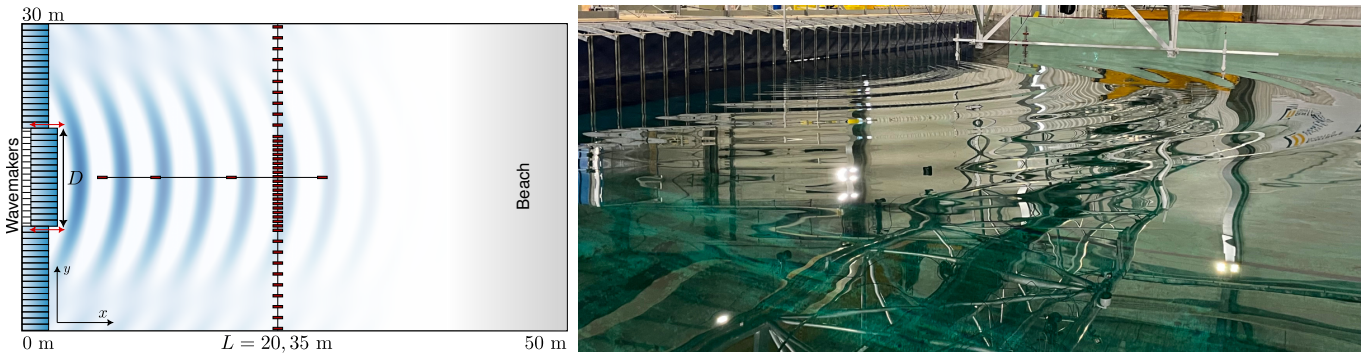

FIG. 1. Experimental set-up. Left: Schematic representation (not to scale) of the 2D water tank (top view) used in the experiments. The transverse profile of the generated waves can be carefully shaped using 48 computer-controlled segmented wavemakers placed along the $y-$axis, at $x = 0$ m. Horizontal red bars: 45 wave elevation probes are placed at discrete propagation distances $x = 1$–25 m and transverse positions $y \in [0.1, 29.64]$ m with a non-uniform spacing, as indicated by the probe array. The wavelength of the carrier wave is approximately $\lambda_c \simeq 1.3$ m. Right: Image of a diffracting wave with an opening of $D = 1.2$ m (i.e., 2 flaps out of 48), see Movies S1 and S2.

how coherent structures evolve and which of their properties persist as departures from one-dimensionality become significant remains an active area of research in nonlinear-wave physics.

Coherent nonlinear structures in 2D wave systems have been reported in different physical contexts, including surface-wave hydrodynamics [32–34], internal waves [35], Marangoni–Bénard convection [36] and more recently, nonlinear optics, where KPI lump solitons were observed in a 2D optical medium [37]. These observations illustrate the continuing relevance of integrable coherent structures beyond strictly 1D settings and motivate experimental investigations of their robustness when additional spatial degrees of freedom become important.

In the present work, we experimentally investigate how deep-water envelope solitons evolve when a controlled transverse degree of freedom is introduced via diffraction. Using a large-scale water tank equipped with independently driven wavemakers, we generate wave packets whose longitudinal profile initially corresponds to a fundamental 1D-NLSE soliton, while their transverse extent is controlled either through a finite aperture or through a Gaussian apodization. This approach provides a systematic way to introduce increasingly strong transverse dynamics while maintaining a well-defined coherent structure in the longitudinal propagation direction. We combine high-resolution measurements, numerical simulations of the HNLSE, and nonlinear spectral analysis based on the IST. We show that the transverse wave-field structure is quantitatively described by classical diffraction theory over a broad range of conditions, while nonlinear spectral analysis simultaneously reveals the persistence of spectral signatures associated with soliton dynamics over a significant portion of the wave field.

I. THEORETICAL BACKGROUND

The quantity of interest in our study, which we measure experimentally, is the surface elevation of water $\eta(x, y, t)$. In the linear regime, 2D surface waves with harmonic time dependence read $\eta(x, y, t) = u(x, y)e^{i\omega t}$, where ω is the angular frequency and satisfies the Helmholtz equation for the spatial envelope $u(x, y)$ as [5, 38]

$$\left(\partial_{xx} + \partial_{yy} + k^2\right) u(x, y) = 0, \tag{1}$$

with $k = 2\pi/\lambda$ the wavenumber.

The diffraction of a monochromatic wave by an aperture located at $x = 0$ is described by the Fresnel–Kirchhoff integral, which in 2D yields the field $u(x, y)$ beyond the aperture as [38]

$$u(x, y) = \int_{-\infty}^{\infty} p(y_0) \left(-\frac{kx}{2i\, r}\right) H_1^{(1)}(kr)\, \mathrm{d}y_0, \tag{2}$$

where $r = \sqrt{x^2 + (y - y_0)^2}$ and $H_1^{(1)}$ is the first-order Hankel function of the first kind, and y_0 is the transverse coordinate along the aperture plane at $x = 0$. The function $p(y_0)$ represents the incident field distribution at the aperture, determined by the slit geometry and, in our experiments, will be imposed by the number of active wavemakers (see Fig. 1). In the numerical evaluation of the integral, we adopt the Kirchhoff approximation, setting $p(y_0) = 1$ within the aperture and $p(y_0) = 0$ outside.

However, at higher wave amplitudes, the linear description breaks down, as nonlinear effects substantially modify wave propagation. Under the assumption of paraxial propagation along the x-direction, the evolution of weakly nonlinear deep-water wave packets is instead governed by the (2D+1) hyperbolic nonlinear Schrödinger equation (HNLSE) [17, 27, 28]. This equation describes the dynamics of the complex envelope $A(x, y, t)$ of a carrier wave with wavenumber k_0 propagating along the x-direction with carrier frequency $\omega_0 = \sqrt{gk_0}$, where g is the gravity acceleration.

$$\partial_x A + \frac{1}{c_g}\partial_t A = -\frac{i}{4k_0}\left(\partial_{xx}A - 2\partial_{yy}A\right) - ik_0^3|A|^2A, \tag{3}$$

where $c_g = \mathrm{d}\omega/\mathrm{d}k\big|_{k_0}$ is the group velocity. The surface elevation $\eta(x, y, t)$ can be approximated to the first order by [28]

$$\eta(x, y, t) = \mathrm{Re}\Big\{A(x, y, t)\, e^{i(k_0 x - \omega_0 t)}\Big\}. \tag{4}$$

At leading order in the weakly nonlinear regime, the envelope propagates at the group velocity c_g, so that $\partial_t A + c_g\partial_x A \simeq 0$ [28, 39]. This relation is used to rewrite the longitudinal second-order dispersive term, while the transport operator $\partial_x + c_g^{-1}\partial_t$ is kept unchanged as it defines the envelope evolution. HNLSE thus reads

$$\partial_x A + \frac{1}{c_g}\partial_t A = -i\left(\frac{1}{g}\partial_{tt}A - \frac{1}{2k_0}\partial_{yy}A\right) - ik_0^3|A|^2A. \tag{5}$$

While the waves remain focusing in the longitudinal direction (as shown below), they are defocusing transversely, raising questions about their stability in the presence of this additional spatial dimension [29, 30]. To explore this regime and compare with experiments, we numerically integrate Eq. (5) (see Supplemental Material [40]), which serves as the principal model throughout this paper. In the weak-amplitude limit, the HNLSE recovers the familiar Fresnel diffraction behaviour associated with transverse wave spreading. The amplitudes considered here, however, extend beyond the strictly linear regime, allowing us to investigate experimentally how nonlinear coherent wave packets evolve in the presence of transverse diffraction.

If the solution is assumed to be independent of the transverse direction y, we recover the (1D+1) focusing nonlinear Schrödinger equation (NLSE), corresponding to purely unidirectional wave propagation along the x-axis, as

$$\partial_x A + \frac{1}{c_g}\partial_t A = -\frac{i}{g}\partial_{tt}A - ik_0^3|A|^2A, \tag{6}$$

which, unlike (3) and (5), is integrable and can be solved through the use of the inverse scattering transform (IST) [19–21]. The well-known fundamental single-soliton solution of (6) can be written as [17, 18, 24],

$$\eta(x, t) = a\ \mathrm{sech}\left[\frac{ak_0\omega_0}{\sqrt{2}}\left(t - \frac{x}{c_g}\right)\right] \times \cos\left[\omega_0 t + k_0\left(1 + \frac{k_0^2a^2}{4}\right)x\right], \tag{7}$$

where a is the maximal soliton envelope amplitude. Within the IST framework, a soliton is characterized by a discrete complex eigenvalue ζ of the associated scattering problem. The imaginary part of this eigenvalue determines the soliton amplitude, while its real part is related to its propagation velocity. The eigenvalue is obtained by solving the corresponding scattering problem (see Supp. Mat. [40]).

II. EXPERIMENTAL SETUP

Experiments were performed in the large-scale wave basin (50 m long × 30 m wide × 5 m deep) of Ecole Centrale de Nantes, France. The experimental setup is sketched in Fig. 1. The wave generation mechanism consists of 48 independently controlled wavemakers (flaps of width 0.62 m, hinged 2.8 m from the free surface) located at one end of the basin, i.e. at $x = 0$. An absorbing, sloping beach is located at the opposite end.

We focus on two types of soliton waveforms, either a slit-diffracting soliton or a Gaussian beam (a soliton with a transverse Gaussian profile along the y-direction, see Fig. 1). Here, the term "slit" will be used in analogy with optical diffraction, as the aperture is implemented by selectively driving a finite set of neighbouring wavemakers. To generate a diffracting soliton, the wavemakers are driven by a monochromatic carrier of fixed frequency $f_0 = 1.1$ Hz [i.e., a fixed carrier wavelength of $\lambda_0 = 2\pi/k_0 = g/(2\pi f_0^2) \simeq 1.3$ m], amplitude-modulated by a hyperbolic secant following the 1D NLSE solitonic solution of (7) at $x = 0$. The carrier wavenumber k_0 is kept fixed, while the soliton maximal

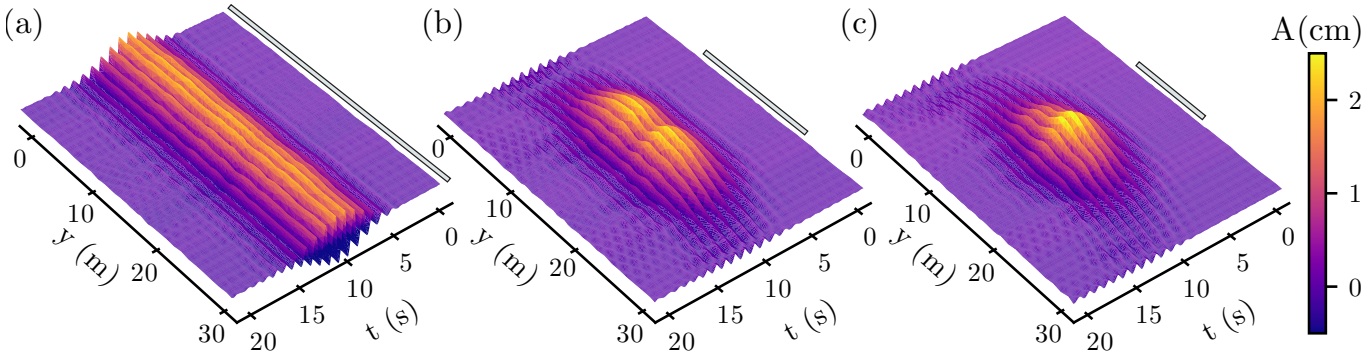

FIG. 2. Measured surface elevation $\eta(y,t)$ of a soliton of steepness $\epsilon = k_0 a = .097$ measured by the wave probes at $L = 20$ m for three different slit openings (see white rectangles) $D = 30$(a),15(b) and 10(c) m. For the largest opening, (a), we observe the classical profile of a 1D NLSE soliton [(7)]. Decreasing the aperture width, as seen in (b) and (c) reduces the transverse (y) size of the soliton, however we still observe a coherent structure in the basin center. Additionally, we observe the appearance of distinct minima and maxima in the transverse profile, consistent with classical wave diffraction.

envelope amplitude a is varied around typical values of $0.4 - 2\,$cm and has a typical size $L_x = gT_0/\omega_0 \in [5.38, 25]$ m, where T_0 is the typical duration of the soliton. The corresponding carrier steepness $\epsilon \equiv k_0 a$ is explored over the range [0.019, 0.044, 0.070, 0.097, 0.127], allowing us to probe regimes from weak to strong nonlinearity. If all wavemakers are driven in phase, a 1D-NLSE soliton with a transverse extension covering the whole width (30 m) of the water tank is generated and propagates towards the beach. By altering the number of working wavemakers, we can change the diffraction aperture, D (see top of Fig. 1), to observe its impact on the soliton propagation and its diffraction. The parameter D is varied from a small 0.6 m aperture to the full 30 m width of the basin.

To generate a Gaussian beam, the carrier wave is now amplitude-modulated along the wavemakers, i.e. in the transverse y-direction. By weighting the driving amplitudes of the different wavemakers, we implement a Gaussian apodization of the initial soliton transverse profile, enabling a controlled smoothing of the aperture edges.

The surface elevation $\eta(t)$ is recorded using an array of 45 resistive wave probes. Of these, 41 are positioned along a straight transverse line located at a selectable distance of either L=20 m or L=35 m from the wavemakers. The probes are spaced 1 m apart, except for the central 23 probes, which are separated by 0.5 m to enhance spatial resolution. The arrangement is shown at the top of Fig. 1. Four additional probes are located in the main propagation direction. The sensors provide a vertical resolution of 0.1 mm, a frequency bandwidth of 20 Hz, and are sampled at 128 Hz. In order to look for the influence of dispersion, diffraction, and nonlinearity in the present configuration, it is useful to introduce the associated characteristic lengths and their range of accessible values in our experiment. The dispersive term in (5) defines the dispersive length $L_{\rm disp} = gT_0^2 \in [141, 3285]$ m. The transverse diffraction term yields a diffraction length $L_{\rm diff} = 2k_0 D^2 \in [9.7, 3895]$ m. Finally, the nonlinear term defines a nonlinear length $L_{\rm NL} = 1/k_0^3 a^2 \in [12.7, 569]$ m. We are thus in a regime where the three typical lengths are comparable in size, and expect both diffractive effects as well as dispersive and nonlinear ones to come into play at the same strength.

III. SLIT DIFFRACTION OF SOLITONS

As described above, we generate wave packets whose longitudinal dynamics correspond to exact single-soliton solutions (7) of the (1D+1) NLSE. By varying the aperture width D, we introduce controlled transverse diffraction. Figure 2 shows the resulting wave field for three different aperture openings. For the maximal opening (Fig. 2a), when all wavemakers are active, the classical NLSE single soliton described by (7) is recovered. As the aperture width is reduced (Fig. 2b–c), the wave packet remains localized while becoming transversely confined to the central region of the basin, over a width consistent with the imposed opening. This is complemented by a now very visible curved wavefront. Additionally, we can notice the emergence of clear maxima and minima in the soliton transverse y-profile, demonstrating the appearance of a diffraction pattern.

These features are more clearly observed in Fig. 3(a1–a5), where the transverse envelope amplitude $A(L, y)$ at a distance $L = 20$ m broadens as the aperture width D increases, while progressively developing the characteristic diffraction pattern with alternating transverse maxima and minima. The measured amplitude profiles (dots) are compared with numerical solutions of (5) (solid lines), showing excellent agreement and confirming that the HNLSE accurately captures soliton diffraction for varying apertures. We further compare the data with the classical Fresnel-Kirchhoff prediction for linear monochromatic waves given by (2) (dashed orange lines) derived from the Helmholtz

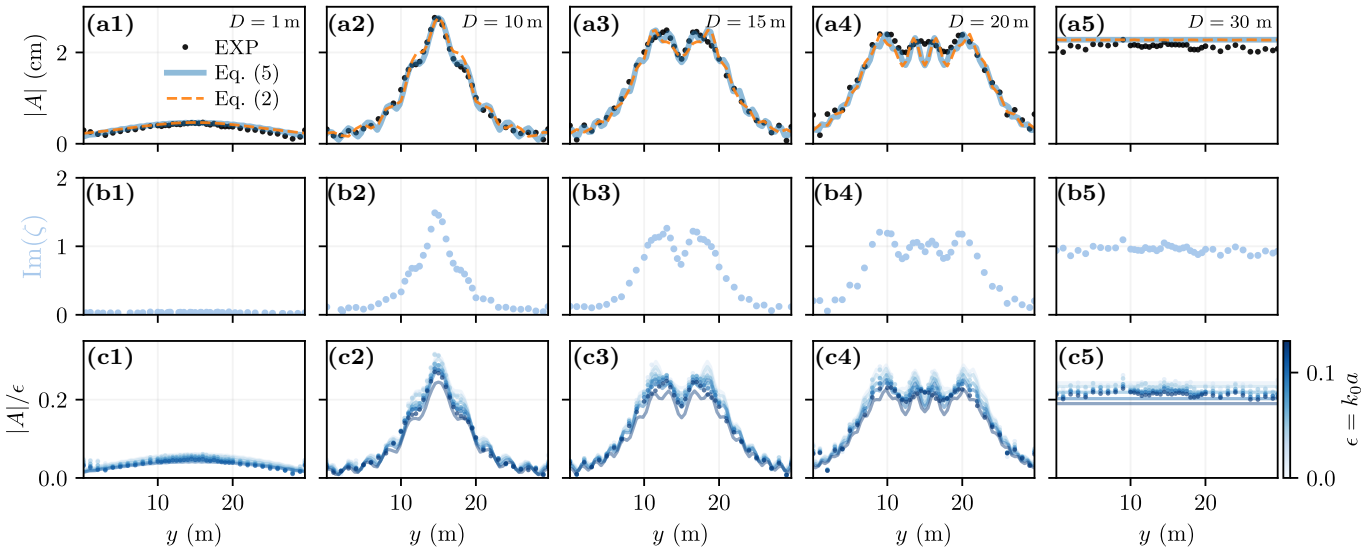

FIG. 3. Transverse structure of diffracting deep-water solitons. Amplitude and IST profiles with comparison with HNLSE and Helmholtz diffraction. The columns correspond to different aperture widths $D = 1$, 10, 15, 20, and 30 m (from left to right), measured at a fixed propagation distance $L = 20$ m. (a1–a5) Transverse envelope amplitude $|A(y)|$. Black dots: experimental data ($\epsilon = 0.097$); solid blue curves: numerical simulations of the HNLSE (5); dashed orange curves (2): linear Helmholtz diffraction by a rectangular slit of width D evaluated for the carrier wavenumber k_0. The Helmholtz predictions are rescaled by a single multiplicative factor to match the experimental peak amplitude in each panel. (b1–b5) IST spectra extracted from the longitudinal wave field and represented as a function of the transverse coordinate y. Blue points correspond to the imaginary part of the discrete eigenvalue, $\mathrm{Im}(\zeta)$, which characterizes the soliton amplitude. The presence of discrete eigenvalue across y indicate the solitonic nature of the wave packet. (c1–c5) Steepness-normalized transverse amplitude $|A(y)|/\epsilon$ for different soliton amplitudes, $a \in [0.37, 2.61]$ cm, generated with the same aperture D. For each run, the experimental curves (markers) and the associated HNLSE profiles (solid curves) are shown for several steepness values $\epsilon = k_0 a \in [0.02, 0.13]$ (the color encodes the soliton steepness, as indicated by the colorbar on the right).

equation. While the generated solitons are well in the nonlinear regime (ϵ up to 0.127), the dominant transverse effects are unexpectedly well captured by the classical linear diffraction limit.

To further elucidate the soliton behavior under slit diffraction, the longitudinal measurements are analyzed using the inverse scattering transform (IST), as detailed in the Supp. Mat. [40]. This approach provides a nonlinear spectral characterization of the (1D+1) NLSE along the longitudinal direction at each transverse position. Unlike envelope measurements alone, the IST yields direct access to the discrete eigenvalues that quantify solitonic content.

The resulting transverse dependence of the discrete complex eigenvalue $\zeta(y)$ is shown in Fig. 3(b1–b5) for the soliton amplitude, i.e., $\mathrm{Im}[\zeta(y)]$. For sufficiently large aperture widths D, well-defined eigenvalues persist across the transverse direction, even as the envelope exhibits pronounced diffraction. This indicates that the finite aperture reshapes the transverse structure of the wavefront without immediately suppressing the nonlinear solitonic content embedded within the longitudinal waveform. In contrast, for small aperture widths (see Fig. 3b1), no discrete eigenvalues are detected, demonstrating the absence of solitonic content. This reveals the existence of a threshold aperture size below which the wave field becomes purely dispersive, and soliton dynamics are lost.

These observations show that, over finite propagation distances and for sufficiently large apertures, transverse diffraction can strongly reshape the wavefront without destroying its longitudinal soliton content. While the wave packet undergoes pronounced 2D deformations, discrete nonlinear spectral signatures associated with soliton dynamics remain observable along the propagation direction. This demonstrates the robustness of coherent structures inherited from the integrable 1D limit, even in the presence of substantial transverse diffraction. The origin of this behavior can be understood physically. In a purely dispersive medium, a wave packet would broaden along the propagation direction, and diffraction at an aperture would generate the superposition of Fresnel patterns associated with its spectral components. Here, however, the IST analysis shows that the wave packet retains its solitonic content: dispersion along x is continuously balanced by nonlinearity, so that the packet remains effectively non-dispersive in the longitudinal direction. Transversely, by contrast, the governing equation is defocusing and does not provide comparable nonlinear self-confinement. The lateral evolution is therefore dominated by diffraction. Because the longitudinal structure remains intact, the transverse field behaves as that of a coherent, non-dispersive object and is accurately described by classical Fresnel diffraction theory derived from the Helmholtz equation. Consequently, the

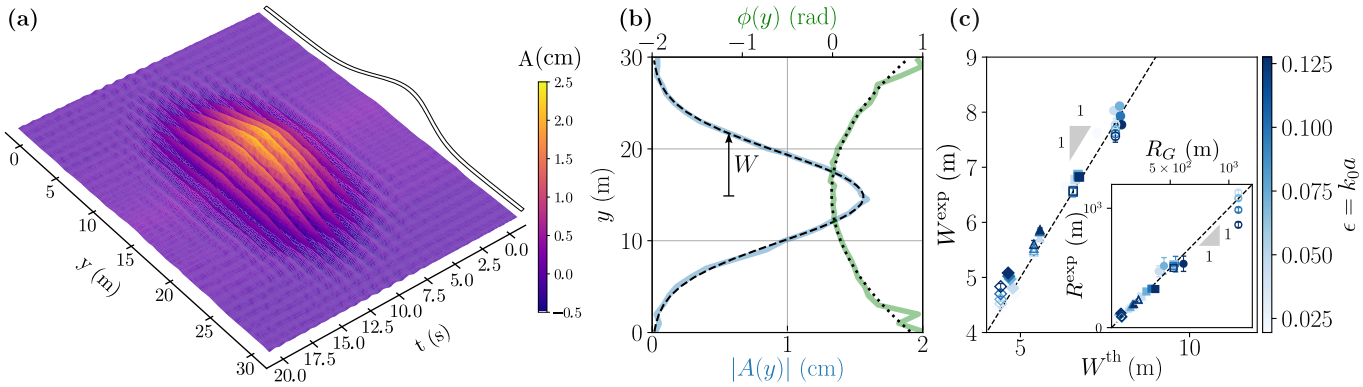

FIG. 4. (a) Measured surface elevation $\eta(y,t)$ of a solitonic Gaussian beam with $\epsilon \approx 0.072$ and waist $W_0 \approx 6.43$ m. The beam is well localized in the transverse direction, and unlike the slit-diffracted soliton, we observe a much more regular wavefront due to the Gaussian apodization (white bar). (b) Transverse cut of a reference soliton at $x = 20$ m, showing the measured envelope amplitude $|A(y)|$ (blue, solid) together with a Gaussian fit (black, dashed), and the corresponding unwrapped transverse phase profile $\phi(y)$ (green, solid) with a parabolic fit (black, dotted), from which the wavefront radius of curvature is extracted. The arrow indicates the fitted transverse waist W of the Gaussian envelope. (c) Measured waist $W^{\rm exp}$ as a function of the theoretical prediction $W^{\rm th}$ ((8)) for different initial waists W_0. Inset: Measured radius of curvature $R^{\rm exp}$ versus the theoretical radius $R_{\rm G}$ ((8)). In panel (c) and its inset, filled symbols correspond to experiments and open symbols to HNLSE simulations. Marker shapes encode different initial waists ($W_0 \approx \diamond 3.87$, $\triangle 5.15$, $\square 6.43$, and $\circ 7.73$ m), while the color scale on the right indicates the soliton steepness $\epsilon = k_0 a$.

soliton undergoes essentially linear transverse diffraction while preserving its nonlinear identity along the direction of propagation.

Finally, we examine the influence of the soliton amplitude on the diffraction pattern, as shown in Fig. 3(c1–c5). The amplitudes $|A(y)|$ are normalized by the wave steepness ϵ and compared with numerical simulations of (5). The resulting diffraction patterns exhibit clear self-similarity across different probed nonlinearities (see right colorbar) and aperture widths D. This invariance indicates that, for sufficiently large D, the longitudinal soliton dynamics remain intact, with transverse diffraction largely independent of the soliton amplitude.

IV. SOLITONS WITH A TRANSVERSE GAUSSIAN PROFILE

In the previous section, diffraction was induced by imposing a sharp transverse truncation of the wavemaker motion, corresponding to the slit geometry. We now move beyond this configuration by importing concepts from Gaussian beam optics to probe soliton diffraction from a different perspective. In optics, Gaussian beams provide a fundamental and analytically tractable description of diffraction and beam spreading [43]. We reproduce this geometry experimentally on the surface of deep water by imposing a Gaussian apodization across the wavemaker array at $x = 0$ and centered on the basin y-axis. The resulting wave field constitutes a genuine hydrodynamic analogue of an optical Gaussian beam, with a crucial distinction: its longitudinal dynamics remain governed by the NLSE and retain a solitonic character, while the transverse envelope is initially Gaussian with waist W_0. This construction allows us to test directly whether the well-established propagation laws of Gaussian beams extend to nonlinear soliton wave packets. An example of the measured elevation of a soliton generated this way is displayed in Fig. 4a, showing a clear localization both in the transverse y-direction, as well as in time, i.e., in the x-direction.

We expect that the evolution of the wavefield follows the standard paraxial Gaussian-beam propagation laws [43]

$$W(x) = W_0\sqrt{1+\left(\frac{x\lambda_0}{\pi W_0^2}\right)^2},\quad R_G(x) = x\left[1+\left(\frac{\pi W_0^2}{x\lambda_0}\right)^2\right], \tag{8}$$

where $W(x)$ is the waist at x extracted from the soliton envelope $|A(x,y)|$, $R_G(x)$ is the radius of curvature inferred from the transverse phase, and λ_0 is the carrier wavelength. Similar propagation laws have been observed experimentally for the manipulation of water waves using electrostriction [44].

We show a measured transverse profile of a Gaussian apodized soliton in Fig. 4b, demonstrating that it indeed retains extremely well a Gaussian form after propagation, both in its amplitude and its phase. The curvature of the wavefront is directly extracted from the transverse phase of the carrier wave, which is locally well described by a quadratic fit

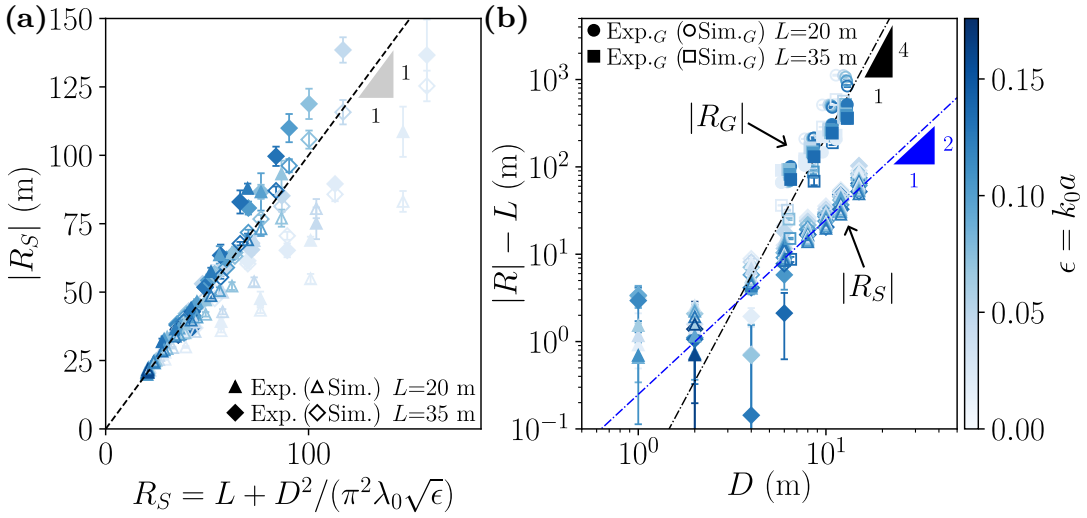

FIG. 5. (a) Absolute value of the soliton wavefront radius of curvature $|R_S|$, extracted from the carrier-wave front, as a function of the rescaled variable $L + D^2/(\pi^2\lambda_0\sqrt{\epsilon})$, where L is the propagation distance, D the transverse aperture (slit) width, λ_0 the carrier wavelength, and $\epsilon = k_0 a$ the steepness. Full (open) symbols denote experiments (HNLSE simulations). Triangles correspond to $L = 20$ m and diamonds to $L = 35$ m. The color encodes ϵ. Error bars indicate the standard deviation over all fits of the individual carrier-wave oscillations. The black dashed line (slope 1) highlights the empirical collapse of (9). (b) (log–log axes): Curvature $|R| - L$ versus D. Circles ($L = 20$ m) and squares ($L = 35$ m) show Gaussian-apodized beams (R_G) extracted from quadratic phase fits (full: experiments; open: HNLSE simulations), with $D = 2W_0\sqrt{\ln 2}$ for five different steepness values. The black dash-dotted line corresponds to (8) with $L = 35$ m and the blue one to the D^2 scaling expected from (9) with $\epsilon = 0.1$. Error bars for these points originate from the uncertainties of the quadratic phase fits, as estimated from the covariance matrix of the fit parameters.

$\phi(y) \simeq \phi_0 + \alpha y^2$ (see dotted line), yielding a radius of curvature $R^{\text{exp}} \equiv k_0(2\alpha)^{-1}$. While such a characterization is standard in the context of Gaussian beams in optics, it is most often obtained indirectly, either from the evolution of the beam waist under the Gaussian-beam assumption [43], or via dedicated wavefront-sensing techniques such as Shack–Hartmann sensors or Talbot–effect methods [45–49] rather than from a direct measurement of the carrier phase. In contrast, our hydrodynamic system provides direct access to the full spatial-temporal wavefield, allowing the curvature of the carrier-wave front to be measured. By repeating measurements for different widths as well as nonlinearities, we confirm in Fig. 4c that such solitons obey perfectly the relationships of (8), both experimentally (full symbols) and numerically (open symbols), giving the first empirical deep-water realization and control of focused Gaussian beams.

V. CURVATURE RADIUS OF A DIFFRACTED SOLITON

Using the direct availability of the wavefront curvature, we use it to further study the slit-diffracted solitons and compare them to Gaussian-apodized solitons. At fixed L, individual wavefront oscillations are locally well captured by a quadratic phase profile in y, from which a curvature radius can be defined (see the procedure illustrated for Gaussian-apodized solitons in Fig. 4b).

Figure 5a shows all curvature measurements for slit-diffracted solitons. Each dataset corresponds to a given propagation distance ($L = 20$ or 35 m), aperture width D, and steepness ϵ, with colors encoding ϵ and open symbols denoting HNLSE simulations. Remarkably, despite such a wide range of parameters, all points align well onto a single straight line of slope 1 (black dashed line) once the abscissa is rescaled according to an empirically obtained nonlinear law

$$R_S = L + \frac{D^2}{\pi^2\lambda\sqrt{\epsilon}}, \tag{9}$$

which, to the best of our knowledge, is a so far unreported relationship. This collapse shows first that the effect of aperture enters predominantly through a quadratic dependence, $R_S - L \propto D^2$. Second, it reveals a strong influence of nonlinearity through the factor $1/\sqrt{\epsilon}$, i.e., at fixed L and D, increasing ϵ decreases R_S, meaning that the wavefront becomes more curved. This trend is consistent with an effective nonlinear focusing of the diffracting wavefront [50, 51].

In other words, while the transverse spreading remains governed by the finite aperture, nonlinear effects modify the local wavefront geometry in this regime.

Figure 5b places this slit-diffracted behaviour (diamond and triangle symbols) in perspective by comparing it to Gaussian-apodized solitons (square and circle symbols, see Sec. IV), where the initial transverse profile is smooth rather than truncated. In that case, as shown in Fig. 4c, both the waist and the curvature follow the standard Gaussian-beam propagation predictions (8), leading to a much stronger dependence on the transverse size, namely $R_G \propto D^4$ since $W_0 = D/(2\sqrt{\ln 2})$. The coexistence of a D^2 scaling for the slit-diffracted soliton R_S and a D^4 scaling for the Gaussian-apodized soliton R_G highlights that the initial transverse shaping at $x = 0$ plays a decisive role in setting the wavefront geometry.

This trend can be interpreted as an effective nonlinear correction to the wavefront curvature, although at present, a theoretical description of the empirical scaling (9) remains an open question.

VI. CONCLUSION

We have investigated how a 1D deep-water envelope soliton evolves when subjected to 2D diffraction. Drawing inspiration from optics, where the transverse profile of a beam is commonly shaped using a slit or Gaussian apodization, we extended this idea to water waves by introducing a controlled transverse degree of freedom while maintaining the longitudinal coherent soliton structure near the wavemakers.

Over the finite propagation distances investigated here, the wave packet retains clear longitudinal solitonic signatures when the aperture is sufficiently large, despite the presence of the additional spatial dimension. While transverse diffraction substantially reshapes the wavefront and is quantitatively captured by classical diffraction theory, nonlinear spectral analysis based on the IST reveals persistent discrete signatures associated with soliton dynamics along the propagation direction. The experiments therefore demonstrate that coherent structures originating from the 1D NLSE remain remarkably robust to the introduction of controlled transverse dynamics.

The robustness of coherent structures under dimensional extension is a central question across many domains, since higher-dimensional effects are known to trigger transverse instabilities [29] or qualitatively modify soliton dynamics [52–54]. This issue is of direct and applicable interest in nonlinear optics and Bose–Einstein condensates, as well as plasma physics and ocean wave dynamics. Our results demonstrate that the transition from integrable 1D dynamics to genuinely 2D behavior is rather progressive than abrupt. More broadly, this controlled experimental platform provides a quantitative framework to explore weakly non-integrable regimes and to test perturbative approaches that attempt to bridge ideal integrable models and realistic nonlinear wave systems [55–59].

ACKNOWLEDGMENTS

We thank A. Levesque, S. Mazo, and B. Pettinotti (ECN) for their technical help on the experimental setup. This work was partially supported by the Agence Nationale de la Recherche through the SOGOOD (Grant No. ANR-21-CE30-0061) project, and the Simons Foundation MPS-WT No. 651463 project. F. C., P. S. and S. R. acknowledge the support of the CDP C2EMPI, as well as the French State under the France-2030 programme, the University of Lille, the Initiative of Excellence of the University of Lille, and the European Metropolis of Lille for their funding and support of the R-CDP-24-004-C2EMPI project. F.N thanks the Humboldt Foundation for a postdoctoral fellowship.

[1] A. Fresnel, Mémoire sur la diffraction de la lumière, Mem. Acad. Roy. Sci. Paris, 339 (1821).
[2] M. Born and E. Wolf, *Principles of optics : electromagnetic theory of propagation, interference and diffraction of light* (Cambridge University Press, 7th Ed., Cambridge 1999).
[3] G. Bekefi, Diffraction of Sound Waves by a Circular Aperture, J. Acoust. Soc. Am **25**, 205 (1953).
[4] A. N. Guz, V. D. Kubenko, and M. A. Cherevko, Diffraction of elastic waves, Sov. Appl. Mech. **14**, 789 (1978).
[5] J. J. Stamnes, *Waves in focal regions: propagation, diffraction and focusing of light, sound and water waves* (Routledge, Abingdon 2017).
[6] R. A. Dalrymple and P. A. Martin, Wave Diffraction Through Offshore Breakwaters, J. Waterw. Port Coast. Ocean Eng. **116**, 727 (1990).
[7] W. G. Penney and A. T. Price, Part I. The diffraction theory of sea waves and the shelter afforded by breakwaters, Phil. Trans. R. Soc. Lond. A **244**, 236 (1952).
[8] R. A. Dalrymple and J. T. Kirby, Models for very wide-angle water waves and wave diffraction, J. Fluid Mech. **192**, 33 (1988).

[9] Y. Goda, T. Takayama, and Y. Suzuki, Diffraction Diagrams for Directional Random Waves, Coastal Engineering Proceedings **1**, 35 (1978).
[10] M. Buccino, S. Tuozzo, and M. Calabrese, The wavefront shift method for bay beaches, Coast. Eng. **199**, 104740 (2025).
[11] F. L. Blue Jr. and J. W. Johnson, Diffraction of water waves passing through a breakwater gap, Eos Trans. AGU **30**, 705 (1949).
[12] J. D. Pos and F. A. Kilner, Breakwater Gap Wave Diffraction: an Experimental and Numerical Study, J. Waterw. Port Coast. Ocean Eng. **113**, 1 (1987).
[13] K. Dysthe, H. E. Krogstad, and P. Müller, Oceanic rogue waves, Annu. Rev. Fluid Mech. **40**, 287 (2008).
[14] M. Onorato, L. Cavaleri, S. Randoux, P. Suret, M. I. Ruiz, M. De Alfonso, and A. Benetazzo, Observation of a giant nonlinear wave-packet on the surface of the ocean, Sci. Rep. **11**, 23606 (2021).
[15] M. Onorato, S. Residori, U. Bortolozzo, A. Montina, and F. T. Arecchi, Rogue waves and their generating mechanisms in different physical contexts, Phys. Rep. **528**, 47 (2013).
[16] C. Kharif, E. Pelinovsky, and A. Slunyaev, *Rogue waves in the ocean* (Springer Science & Business Media, Berlin 2008).
[17] V. E. Zakharov, Stability of periodic waves of finite amplitude on the surface of a deep fluid, J. Appl. Mech. Tech. Phys. **9**, 190 (1968).
[18] M. Remoissenet, *Waves called solitons: concepts and experiments* (Springer Science & Business Media, Berlin 2013).
[19] M. J. Ablowitz, D. J. Kaup, A. C. Newell, and H. Segur, Nonlinear-evolution equations of physical significance, Phys. Rev. Lett. **31**, 125 (1973).
[20] S. Novikov, S. V. Manakov, L. P. Pitaevskii, and V. E. Zakharov, *Theory of solitons: the inverse scattering method* (Springer Science & Business Media, New York 1984).
[21] J. Yang, *Nonlinear waves in integrable and nonintegrable systems* (SIAM, Philadelphia 2010).
[22] F. Bonnefoy, A. Tikan, F. Copie, P. Suret, G. Ducrozet, G. Prabhudesai, G. Michel, A. Cazaubiel, E. Falcon, G. El, and S. Randoux, From modulational instability to focusing dam breaks in water waves, Phys. Rev. Fluids **5**, 034802 (2020).
[23] P. Suret, A. Tikan, F. Bonnefoy, F. Copie, G. Ducrozet, A. Gelash, G. Prabhudesai, G. Michel, A. Cazaubiel, E. Falcon, G. El, and S. Randoux, Nonlinear Spectral Synthesis of Soliton Gas in Deep-Water Surface Gravity Waves, Phys. Rev. Lett. **125**, 264101 (2020).
[24] A. Cazaubiel, G. Michel, S. Lepot, B. Semin, S. Aumaître, M. Berhanu, F. Bonnefoy, and E. Falcon, Coexistence of solitons and extreme events in deep water surface waves, Phys. Rev. Fluids **3**, 114802 (2018).
[25] G. Michel, F. Bonnefoy, G. Ducrozet, G. Prabhudesai, A. Cazaubiel, F. Copie, A. Tikan, P. Suret, S. Randoux, and E. Falcon, Emergence of Peregrine solitons in integrable turbulence of deep water gravity waves, Phys. Rev. Fluids **5**, 082801 (2020).
[26] L. Fache, F. Bonnefoy, G. Ducrozet, F. Copie, F. Novkoski, G. Ricard, G. Roberti, E. Falcon, P. Suret, G. El, and S. Randoux, Interaction of soliton gases in deep-water surface gravity waves, Phys. Rev. E **109**, 034207 (2024).
[27] J.-M. Ghidaglia and J.-C. Saut, Nonelliptic Schrödinger equations, J. Nonlinear Sci. **3**, 169 (1993).
[28] A. R. Osborne, *Nonlinear ocean wave and the inverse scattering transform* (Academic Press, San Diego 2010).
[29] V. E. Zakharov and A. M. Rubenchik, Instability of waveguides and solitons in nonlinear media, Zh. Eksp. Teor. Fiz **65**, 997 (1973).
[30] B. Deconinck, D. E. Pelinovsky, and J. D. Carter, Transverse instabilities of deep-water solitary waves, Proc. R. Soc. A **462**, 2039 (2006).
[31] M. J. Ablowitz and J. T. Cole, Transverse Instability of Rogue Waves, Phys. Rev. Lett. **127**, 104101 (2021).
[32] H. Yeh, W. Li, and Y. Kodama, Mach reflection and KP solitons in shallow water, The European Physical Journal Special Topics **185**, 97 (2010).
[33] M. J. Ablowitz and D. E. Baldwin, Nonlinear shallow ocean-wave soliton interactions on flat beaches, Phys. Rev. E **86**, 036305 (2012).
[34] T. Leduque, M. Kaczmarek, H. Michallet, E. Barthélemy, and N. Mordant, From deep to shallow water two-dimensional wave turbulence: Emergence of soliton gas, Phys. Rev. Fluids **10**, 114801 (2025).
[35] T. Maxworthy, On the formation of nonlinear internal waves from the gravitational collapse of mixed regions in two and three dimensions, J. Fluid Mech. **96**, 47 (1980).
[36] P. D. Weidman, H. Linde, and M. G. Velarde, Evidence for solitary wave behavior in Marangoni–Bénard convection, Physics of Fluids A: Fluid Dynamics **4**, 921 (1992).
[37] L. Dieli, D. Pierangeli, F. Baronio, S. Trillo, and C. Conti, Observation of lump solitons, Phys. Rev. Lett. **136**, 053804 (2026).
[38] J. J. Stamnes, Focusing of two-dimensional waves, J. Opt. Soc. Am. **71**, 15 (1981).
[39] A. Chabchoub, K. Mozumi, N. Hoffmann, A. V. Babanin, A. Toffoli, J. N. Steer, T. S. van den Bremer, N. Akhmediev, M. Onorato, and T. Waseda, Directional soliton and breather beams, Proc. Natl. Acad. Sci. U.S.A. **116**, 9759 (2019).
[40] See Supplemental Material at [URL will be inserted by publisher] for details on I. numerical integration of the 2D NLS, II. IST spectrum and experimental data, III. phase profiles of the diffracted solitons, IV. equivalence of phase curvature and wavefront curvature profiles, V. movies.
[41] E. Hairer, G. Wanner, and S. P. Nørsett, *Solving ordinary differential equations I: Nonstiff problems* (Springer, Berlin 1993).
[42] A. Shabat and V. Zakharov, Exact theory of two-dimensional self-focusing and one-dimensional self-modulation of waves in nonlinear media, Sov. Phys. JETP **34**, 62 (1972).
[43] O. Svelto and D. C. Hanna, *Principles of lasers* (Springer, Berlin 2010).
[44] V. Mouet, B. Apffel, and E. Fort, Comprehensive refractive manipulation of water waves using electrostriction, Proc. Natl.

Acad. Sci. U.S.A. **120**, e2216828120 (2023).
[45] D. R. Neal, W. J. Alford, J. K. Gruetzner, and M. E. Warren, Amplitude and phase beam characterization using a two-dimensional wavefront sensor, Third International Workshop on Laser Beam and Optics Characterization **2870**, 72 (1996).
[46] V. Y. Zavalova and A. V. Kudryashov, Shack-Hartmann wavefront sensor for laser beam analyses, High-Resolution Wavefront Control: Methods, Devices, and Applications III **4493**, 277 (2002).
[47] D. Thul, M. Richardson, and S. Rostami Fairchild, Spatially resolved filament wavefront dynamics, Sci. Rep. **10**, 8920 (2020).
[48] A. Goloborodko, Wavefront curvature restoration by a sensor based on the Talbot phenomenon under Gaussian illumination, J. Opt. Soc. Am. A **40**, B8 (2023).
[49] M. M. Kotov, V. P. Danko, and A. O. Goloborodko, Talbot wavefront sensor measurement possibilities under gaussian illumination, Opt. Lasers Eng. **169**, 107718 (2023).
[50] V. E. Zakharov, Instability of self-focusing of light, Sov. Phys. JETP **26**, 994 (1968).
[51] S. A. Akhmanov, A. P. Sukhorukov, and R. V. Khokhlov, Self-focusing and diffraction of light in a nonlinear medium, Sov. Phys. Uspekhi. **10**, 609 (1968).
[52] Y. S. Kivshar and D. E. Pelinovsky, Self-focusing and transverse instabilities of solitary waves, Phys. Rep. **331**, 117 (2000).
[53] K. D. Moll, A. L. Gaeta, and G. Fibich, Self-similar optical wave collapse: observation of the Townes profile, Phys. Rev. Lett. **90**, 203902 (2003).
[54] C. Sulem and P.-L. Sulem, *The nonlinear Schrödinger equation: self-focusing and wave collapse* (Springer Science & Business Media, New York 2007).
[55] D. J. Kaup, A perturbation expansion for the Zakharov–Shabat inverse scattering transform, SIAM J. Appl. Math. **31**, 121 (1976).
[56] V. I. Karpman and E. M. Maslov, Perturbation theory for solitons, Zh. Eksp. Teor. Fiz **73**, 537 (1977).
[57] Y. S. Kivshar and B. A. Malomed, Dynamics of solitons in nearly integrable systems, Rev. Mod. Phys. **61**, 763 (1989).
[58] A. Gelash, S. Dremov, R. Mullyadzhanov, and D. Kachulin, Bi-solitons on the surface of a deep fluid: An inverse scattering transform perspective based on perturbation theory, Phys. Rev. Lett. **132**, 133403 (2024).
[59] L. Falsi, A. Villois, F. Coppini, A. J. Agranat, E. DelRe, and S. Trillo, Evidence of $1+1$D Photorefractive Stripe Solitons Deep in the Kerr Limit, Phys. Rev. Lett. **133**, 183804 (2024).

Supplementary material for Diffraction of deep-water solitons

Filip Novkoski,[1,2,*] Loïc Fache,[1,3,†] Félicien Bonnefoy,[4] Guillaume Ducrozet,[4] Jason Barckicke,[1] François Copie,[3] Pierre Suret,[3] Eric Falcon,[1] and Stéphane Randoux[3]

[1] *Université Paris Cité, CNRS, Matière et systèmes complexes, F-75013 Paris, France*
[2] *PULS, Institute for Theoretical Physics, FAU Erlangen-Nürnberg, 91058, Erlangen, Germany*
[3] *Univ. Lille, CNRS, UMR 8523 - PhLAM - Physique des Lasers Atomes et Molécules, F-59 000 Lille, France*
[4] *Nantes Université, École Centrale Nantes, CNRS, LHEEA, UMR 6598, F-44 000 Nantes, France*

INTEGRATION OF THE 2D NLSE

We integrate numerically the hyperbolic (2D+1) NLSE [Eq. (5) of the main text], written in the retarded-time frame, for the complex envelope $A(x,t,y)$ using a pseudo-spectral scheme in the (t,y) plane. The field is discretized on a rectangular periodic domain $t \in [-L_t/2, L_t/2]$, $y \in [-L_y/2, L_y/2]$ with uniform grids of size $N_t \times N_y$; derivatives ∂_{tt} and ∂_{yy} are evaluated in Fourier space using fast Fourier transforms, while the cubic term $|A|^2A$ is computed in physical space. In the simulations we use, $L_t = 80$ s, and $L_y = 110$ m with $N_t = 512$ and $N_y = 256$ grid points. The resulting system of ordinary differential equations in the propagation variable x is advanced with an explicit adaptive Runge–Kutta integrator (DOP853) [1]. The initial condition reproduces the experimental forcing as a soliton waveform, with a transverse profile (super-Gaussian, Gaussian or other) matching the experimental aperture. Parameters are set by the experimental carrier frequency ($k_0 = \omega_0^2/g$) and steepness $\epsilon = k_0 a$.

THE IST SPECTRUM OF EXPERIMENTAL DATA

For a solution of the nonlinear Schrödinger equation (NLSE) comprising N solitons, the discrete spectrum consists of N complex eigenvalues ζ_n, each associated with a complex norming constant C_n that characterizes the corresponding phase. Collectively, these quantities constitute the complete set of scattering data for the solution.

The discrete spectrum is determined by solving the eigenvalue problem associated with the Lax pair formulation of the NLSE. Each eigenvalue admits a direct physical interpretation: its real part corresponds to the soliton velocity, while its imaginary part determines the soliton amplitude.

In the focusing case of the NLSE, the associated eigenvalue problem reduces to the Zakharov–Shabat spectral problem [2],

$$\hat{\mathcal{L}}\,\Phi = \zeta\,\Phi, \qquad \hat{\mathcal{L}} = \begin{pmatrix} i\partial_\xi & -i\psi \\ -i\psi^* & -i\partial_\xi \end{pmatrix}, \tag{1}$$

where $\Phi(\xi,\zeta)$ is a vector wave function. $\zeta \in \mathbb{C}$ represent the eigenvalues composing the discrete spectrum associated with the soliton content of the field $\psi(\tau,\xi)$ that is measured at some given evolution time τ (or propagation distance x in the experiment) and at each y-coordinate. Connection between the physical envelope $A(x,t)$ and the dimensionless variables used in the problem of (1) is given by, $\tau = xk_0^3a^2/8$, $\xi = \sqrt{k_0^2\omega_0^2a^2/8}\left(t - \frac{x}{c_g}\right)$ and $\psi(\tau,\xi) = A(x,t)/(a/2)$, see [3, 4].

We reconstruct the slowly varying complex envelope $A(x;y)$ from the surface elevation $\eta(x,t;y)$ by demodulating the carrier wave at frequency ω_0 and wavenumber k_0 through the use of the Hilbert transform, yielding both the amplitude and phase of the envelope. The envelope is then rescaled using the standard deep-water NLSE normalization given above. For each transverse position y, the reconstructed envelope $A(x;y)$ is treated as an initial condition of the Zakharov-Shabat spectral problem (1). The Zakharov-Shabat problem is then solved numerically for each transverse position y using the Fourier collocation method, following the procedure described in [5] and previously successfully used experimentally in [3, 4].

* filip.novkoski@fau.de
† loic-joseph.fache@u-pariscite.fr

PHASE PROFILES OF THE SLIT-DIFFRACTED SOLITONS

In the main text (Fig. 3) we focused on the transverse envelope amplitude $|A(y)|$ of the diffracting deep-water soliton and showed that it is accurately described by both the HNLSE simulations (Eq. (5) in the main text) and the linear diffraction theory derived from the Helmholtz equation (Eq. (2) in the main text).

Here we complement this analysis by examining the corresponding transverse phase structure of the wavepacket. While the amplitude determines the spatial broadening of the wavepacket, the phase contains information about the curvature of the wavefront due to the diffraction.

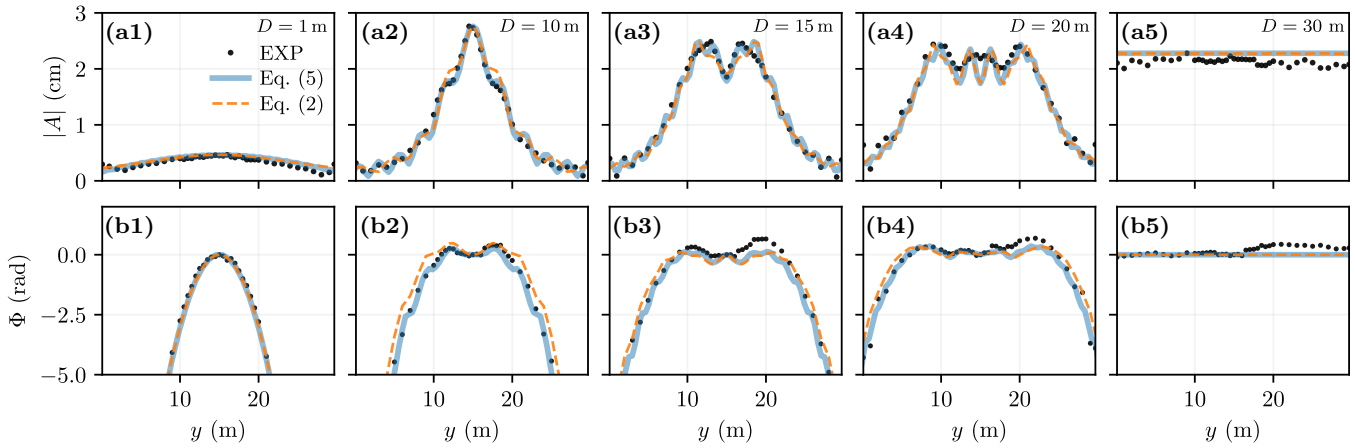

FIG. 1. Transverse amplitude and phase profiles of diffracting deep-water solitons. Columns correspond to different effective aperture (slit) widths $D = 1, 10, 15, 20$, and 30 m measured at the propagation distance $L = 20$ m (same experimental runs as in Fig. 3 of the main text). Black dots show the experimental data extracted along the ridge of maximum amplitude in the (y, t) plane. Solid blue curves correspond to HNLSE simulations (Eq. (5) in the main text), while dashed orange curves show the prediction of the linear Fresnel-Kirchhoff diffraction model (Eq. (2) in the main text). The phase is referenced to the central position $\Phi(y_0) = 0$.

The phase profiles are extracted from the experimentally reconstructed complex wave field using the same procedure as in the main text. Because the wavepacket propagates with finite curvature, the maximum of the envelope does not occur at a constant time t for all transverse positions y. Instead, the crest of maximum amplitude in the (y, t) plane is weakly curved.

To account for this effect, the crest is approximated by a parabolic curvature,

$$t(y) = t_{\text{peak}} + \beta(y - y_0)^2 \tag{2}$$

where t_{peak} denotes the time of maximum amplitude near the center of the packet (y_0), and β characterizes the curvature of the crest.

The transverse phase profile is then obtained from the complex field $A(y, t)$ as

$$\Phi(y) = \arg\left[A\big(y, t(y)\big)\right] \tag{3}$$

The phase is then unwrapped and referenced to the central position y_0 such that $\Phi(y_0) = 0$. Figure S1(b1–b5) shows the resulting phase profiles together with the predictions of the HNLSE simulations (Eq. (5) in the main text) and of the linear Fresnel-Kirchhoff diffraction model (Eq. (2) in the main text). The Fresnel-Kirchhoff prediction is obtained by evaluating the diffraction integral described in the main text for a rectangular aperture of width D, using the carrier wavenumber k_0 and the experimental propagation distance L.

The experimental phase profiles display a clear transverse curvature ($\sim 1/R_S$) that increases as the aperture width D decreases, consistent with stronger diffraction. As observed for the amplitude profiles in Fig. 3 of the main text, the Fresnel-Kirchhoff diffraction model provides an excellent description.

Unlike the case of Gaussian beams, whose transverse phase is strictly parabolic due to the quadratic phase factor associated with a single radius of curvature (see Fig. 4 in the main text), the phase resulting from slit diffraction is not described by a single quadratic form. Instead, the field results from the coherent superposition of contributions emitted by all points of the aperture according to the Fresnel–Kirchhoff principle. As a result, the transverse phase profile deviates from a purely parabolic dependence and exhibits a non-uniform local curvature, particularly visible near the

central region of the packet. For this reason, the radius of curvature measurements reported in the main text for the slit configuration R_S (see Fig. 5 in the main text) were restricted to experiments with aperture widths $D < 12$ m, where the transverse phase does not develop extended plateaus of nearly constant phase. For larger apertures, diffraction becomes weaker and the phase profile approaches a quasi-uniform distribution, making a reliable determination of the radius of curvature ill-defined.

EQUIVALENCE PHASE CURVATURE AND WAVEFRONT CURVATURE PROFILES

In the main text, the radius of curvature of the diffracted soliton wavefront R_S was determined from the geometry of the carrier-wave oscillations in the space-time field representation. Here, we show that the same curvature can also be obtained directly from the transverse phase profile of the reconstructed complex field, following the same procedure used for the apodized solitons in the main text to determine R_G.

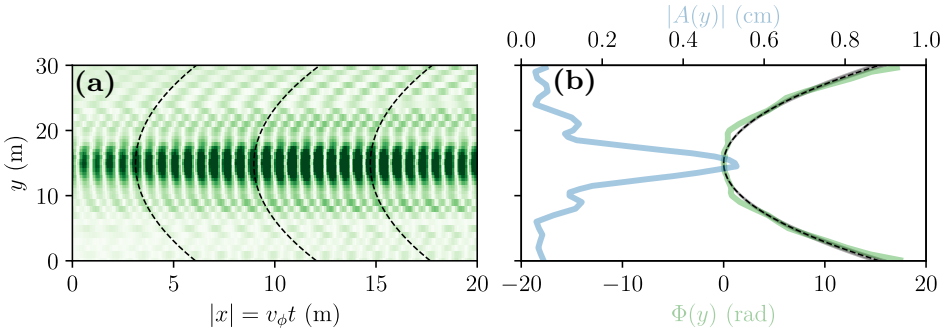

FIG. 2. Consistency between wavefront curvature measurements obtained from carrier-wave oscillations and from the transverse phase profile. The data correspond to a soliton diffracted by a slit of width $D = 6$ m at a propagation distance $L = 20$ m with steepness $\epsilon = k_0 a = 0.021$. (a) Space–time evolution of the carrier-wave amplitude as a function of the transverse coordinate y and propagation coordinate $|x| = v_\phi t$, $v_\phi = \omega_0/k_0$ being the phase-velocity. The dashed curves show parabolic fits of the carrier-wave maxima, used in the main text to determine the wavefront radius of curvature R_S. (b) Transverse phase profile $\Phi(y)$ (green, bottom axis) and amplitude profile $|A(y)|$ (blue, top axis) extracted from the experimentally reconstructed complex field. The dashed curve corresponds to the quadratic phase profile expected for a wavefront of curvature R_S, $\Phi(y) = k_0(y - y_0)^2/(2R_S)$, where R_S is obtained from the carrier-wave fits shown in (a). The shaded region indicates the uncertainty associated with the curvature estimate.

To estimate the wavefront radius of curvature from the experimental measurements, the carrier-wave maxima are detected in the $(|x|, y)$ plane, as illustrated in Fig. S2a. This directly provides an estimate of the wavefront radius of curvature R_S (see main text). Independently we extract the phase of the complex field and its transverse profile $\Phi(y)$ is computed, as shown in Fig. S2b. For a spherical wavefront with radius of curvature R_S, the phase is expected to follow the quadratic dependence

$$\Phi(y) \simeq \frac{k_0}{2R_S}(y - y_0)^2$$

Figure S2 compares the phase profile measured experimentally (green curve) with the quadratic phase predicted using the curvature R_S obtained from the carrier-wave analysis (black dashed line). The excellent agreement between the two curves demonstrates the consistency of the two measurement methods.

I. MOVIES

Movie 1 Diffraction of a deep-water soliton through a slit of width $D = 6$ m. Experimental visualization from behind the wavemakers of a deep-water soliton diffracting after passing a transverse aperture (slit). The video shows the water elevation in the wave basin during one experiment. After the generation, the soliton envelope progressively broadens in the transverse direction due to diffraction, while the longitudinal structure of the packet remains a soliton. The curved wavefront associated with diffraction can be clearly seen in the carrier-wave oscillations.

Movie 2 Diffraction of a deep-water soliton through a slit of width $D = 20$ m. Experimental visualization of a deep-water soliton diffracting after passing a transverse aperture (slit). The video shows the water elevation in the wave basin during one experiment. After the generation, the soliton envelope progressively broadens in the transverse direction due to diffraction, while the longitudinal structure of the packet remains a soliton. Due to the large slit opening, it can be seen that the wavefront experiences a large radius of curvature.

[1] E. Hairer, G. Wanner, and S. P. Nørsett, *Solving ordinary differential equations I: Nonstiff problems* (Springer, 1993).

[2] A. Shabat and V. Zakharov, Exact theory of two-dimensional self-focusing and one-dimensional self-modulation of waves in nonlinear media, Sov. Phys. JETP **34**, 62 (1972).

[3] P. Suret, A. Tikan, F. Bonnefoy, F. Copie, G. Ducrozet, A. Gelash, G. Prabhudesai, G. Michel, A. Cazaubiel, E. Falcon, G. El, and S. Randoux, Nonlinear spectral synthesis of soliton gas in deep-water surface gravity waves, Phys. Rev. Lett. **125**, 264101 (2020).

[4] L. Fache, F. Bonnefoy, G. Ducrozet, F. Copie, F. Novkoski, G. Ricard, G. Roberti, E. Falcon, P. Suret, G. El, and S. Randoux, Interaction of soliton gases in deep-water surface gravity waves, Phys. Rev. E **109**, 034207 (2024).

[5] J. Yang, *Nonlinear waves in integrable and nonintegrable systems* (SIAM, 2010).